photonics

MDPI

Article

UAV Target Enhancement for PPM-Coded Free-Running Single-Photon Range Imaging in Building Background

Yufei Wei [1,2], Xuehe Zheng [3], Rui Yao [2], Jia Guo [4], Ziyi Tong [4], Zhen Yang [4], Jianlong Zhang [4] and Yong Zhang [4,*]

[1] School of Information and Electronics, Beijing Institute of Technology, Beijing 100081, China
[2] Beijing Institute of Electronic System Engineering, Beijing 100854, China
[3] China Changfeng Mechanics and Electronics Technology Academy, Beijing 100854, China
[4] Department of Optoelectronic Information Science and Technology, Harbin Institute of Technology, Harbin 150080, China
* Correspondence: zzyyyy@hit.edu.cn

Abstract

Single-photon detection is a promising approach for low–slow–small Unmanned Aerial Vehicle (UAV) detection, holding great value in urban air defense and security monitoring. In complex urban environments, intense non-uniform building clutter and multi-echo aliasing easily submerge weak target signals, severely limiting traditional single-photon systems under low signal-to-background ratios. To address this, this paper proposes an urban-oriented detection strategy based on a free-running single-photon array, and designs a dual-optimized pulse position modulation laser detection and range image enhancement algorithm. By establishing temporal correlations via pulse sequence convolution, the algorithm effectively isolates weak UAV echoes from strong background clutter to break through detection limitations. Compared with the popular Markov correction method that often suppresses overlapping weak targets under strong reflections, the proposed method significantly improves small-target feature retention, successfully balancing background elimination and detection sensitivity. Field tests and quantitative evaluations demonstrate that the system reliably eliminates building clutter and achieves stable continuous tracking of weak UAV signals within 1.5 km, providing a highly robust and effective technical solution for urban low-altitude surveillance.

Keywords: single-photon detection; PPM LiDAR; UAV detection; range image enhancement

1. Introduction

With the rapid proliferation of low-altitude unmanned aerial vehicle technologies, unauthorized UAV flights in urban and airport core zones have grown frequently, seriously threatening airspace security and key-area protection [1]. Such UAVs present low observability, and dense architectural clutter further hinders reliable detection using conventional methods. Benefiting from single-photon-level sensitivity and high temporal resolution, single-photon LiDAR provides a promising solution for detecting low-reflectivity and small-cross-section targets [2–4].

A series of advanced reconstruction algorithms have been developed to improve the imaging performance of single-photon detection systems under low-photon and high-noise conditions [5]. Representative methods include Bayesian inference-based first-photon imaging [6], array-based maximum likelihood estimation [7–10], adaptive filtering [11,12], and statistical reconstruction algorithms for SPAD detectors [13,14]. These techniques effectively suppress Poisson noise, restore target distance and intensity information, and

Check for updates

Received: 19 May 2026
Revised: 22 June 2026
Accepted: 23 June 2026
Published: 25 June 2026

Copyright: © 2026 by the authors. Licensee MDPI, Basel, Switzerland. This article is an open access article distributed under the terms and conditions of the Creative Commons Attribution (CC BY) license.

enhance weak-signal detection capability by utilizing spatial photon correlation, total variation constraints, dynamic time-window adjustment, and multi-frame fusion strategies. Despite these advancements, most existing algorithms are designed for general static scenes and customized for gated-mode detectors. They lack targeted optimization for dense architectural clutter and fast-moving tiny targets, making it difficult to separate weak UAV echoes from intensive building scattering [15] and limiting the practical engineering application of single-photon LiDAR in complex clutter scenarios [16–19].

To address the problem that UAV echoes are easily submerged by strong building clutter and conventional single-photon systems suffer from poor detection stability and high false alarm rates, this paper proposes a UAV detection method based on a free-running single-photon array [20]. The adopted free-running detection mode eliminates gating time constraints and improves weak-target capture efficiency with a short dead time, mitigating near-field clutter interference [21]. Meanwhile, pseudo-random pulse position modulation (PPM) is applied to laser transmitting. Considering the high correlation between coded laser sequences and target echoes while background signals remain uncorrelated, weak target signals are extracted through sequence convolution. Furthermore, an adaptive range imaging enhancement algorithm is designed, which combines local outlier detection, temporal constraints and cell averaging constant false alarm rate to suppress building clutter and enhance UAV imaging quality [22]. In contrast to the currently popular Markov correction methods [23] that preferentially reconstruct large-scale background structures and tend to bury weak UAV targets within multi-echo overlapping regions, the proposed strategy focuses on small-target feature retention to preserve weak echoes against intense reflections. Experimental results verify that the proposed method can effectively separate UAV echoes from intense architectural clutter under ultra-low Signal-to-Background Ratio (SBR), thereby significantly improving UAV detection probability.

2. Enhanced PPM-Coded Free-Running Single-Photon Imaging

2.1. Free-Running Single-Photon Detection Mechanism for Weak UAV Echoes

The principle of a free-running single-photon detection system is shown in Figure 1, which mainly consists of three modules: a transmitter module, a receiver module, and a signal processing module [24,25]. The transmitter module is responsible for emitting modulated pulsed laser beams toward the target area; the receiver module synchronously detects reflected echoes from the target surface and ambient stray light, and converts optical signals into corresponding electrical signals through photoelectric conversion devices; and the signal processing module further receives the electrical signals and measures the target distance by calculating the time interval between transmitted pulses and received echoes based on the time-of-flight ranging principle [26,27].

A low-altitude flying UAV is a typical non-cooperative point target for LiDAR systems, usually occupying only a single pixel in imaging. According to the LiDAR equation for non-cooperative point targets, the single-pulse laser echo energy can be given as:

$$E_R = \frac{E_T \eta_T \eta_\tau \eta_q \rho A_T A_s T_a^2 D^2}{4\theta^2 R^4}, \quad (1)$$

where E_T is the single-pulse laser energy, η_T is the transmittance of the transmitting optical system, η_τ is the transmittance of the receiving optical system, η_q is the quantum efficiency of the single-photon detector, ρ is the target surface reflectivity, A_T is the effective receiving area of the receiving optical system, A_s is the target reflection area, $h\nu$ is the energy of a single photon in the transmitted laser pulse, θ is the divergence angle of the transmitted laser, R is the distance between the LiDAR system and the target, Ta^2 is the square of the

one-way atmospheric transmittance, and D is the receiving aperture size. Based on this, the number of single-pulse echo photons can be derived as:

$$n_s = \frac{E_T}{h\nu} \cdot \frac{\eta_T \eta_\tau \eta_q \rho A_T A_s T_a^2 D^2}{4\theta^2 R^4}. \tag{2}$$

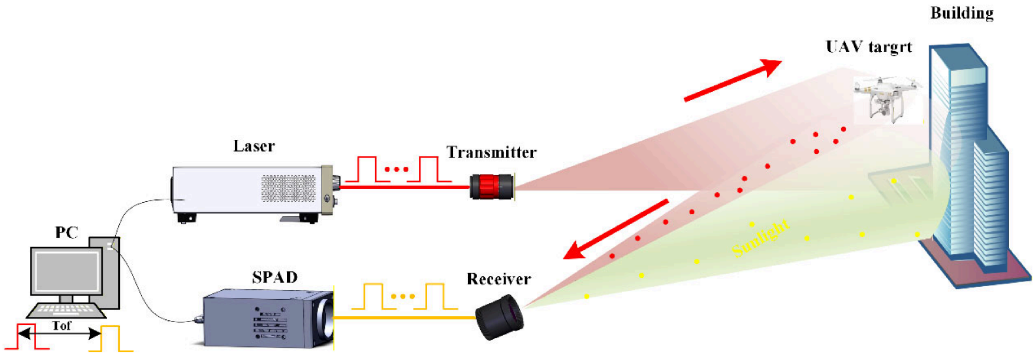


Figure 1. The principle of a free-running single-photon detection system. Red lines denote transmitted laser pulses, yellow lines represent echo photon signals received by SPAD; the ellipsis indicates continuous repeated pulse sequences. The bidirectional red arrows show the laser propagation path, red dots stand for target reflected echo photons, and yellow dots are solar background noise photons.

Background noise consists of ambient radiation, building scattering, and detector dark counts [28,29]. The average number of background photons is given by:

$$n_n = \frac{\eta_q \int_0^{\Delta t} \eta_r \Omega_R I_{bk} d_\tau}{h\nu} + n_b, \tag{3}$$

where n_b is the detector dark count. Furthermore, given a transmitted signal waveform $s(t)$, the received signal $r(t)$ can be expressed as [30]:

$$r(t) = \eta s(t - \frac{2R}{c}) + b, \tag{4}$$

Here, η is the total link efficiency of the system, c is the speed of light, R is the target distance, and b is the background noise intensity.

Since single-photon detection follows an approximate Poisson distribution under weak light conditions, define the background noise intensity as B and the transmitted signal intensity as S within one detection period, where η_d is the detector quantum efficiency and d the detector dark count. According to the Poisson distribution, the probability of no photons being detected is:

$$P_0 = \exp[-(\eta_d \eta_0 S + B)]. \tag{5}$$

For a free-running single-photon detector with dead time, the detector cannot record photon response events when in the dead-time state [31,32]. This characteristic causes temporal correlation of photon detection events, forming a Markov chain process. For a detector with dead time t_d, the photon detection probability $P(t)$ varying with time t can be expressed as [33,34]:

$$P(t) = \left(1 - \int_{t-t_d}^{t} P_0(t)dt\right) P_0(t), \tag{6}$$

where $P_0(t)$ denotes the detection probability of an ideal detector without dead time.

Under strong background noise conditions, the background noise term B in Equation (5) increases drastically, which significantly raises the ideal dead-time-free detection probability $P_0(t)$. Substituting into Equation (6), the integral $\int_{t-t_d}^{t} P_0(t)$ rapidly approaches unity, driving the pre-constraint factor $1 - \int_{t-t_d}^{t} P_0(t)$ to converge to zero. The near-zero value of this constraint factor leads to a sharp drop in the actual dead-time-limited detection probability $P(t)$ and induces counting saturation distortion. In this case, the effective

detection probability corresponding to ranging echo signals is severely suppressed, and target photons can hardly be captured by the detector. Echoes from weak targets are readily submerged by massive background noise, generating numerous noise-induced false distance peaks during imaging and severely degrading target identification and ranging performance.

In single-photon detection systems, the probability of capturing a real target with a single pulse is often low. In practical engineering, multi-pulse statistical accumulation is usually adopted to improve the final detection confidence. Suppose the system requires the final cumulative detection probability of a real target to reach P_D, and each laser pulse detection process is independent. If the detector successfully records a real target with a probability P_{hit} in a single pulse, after N pulse accumulations, the probability of successfully detecting the target at least once satisfies:

$$P_D = 1 - (1 - P_{hit})^N. \tag{7}$$

From this, the minimum theoretical number of detections N_{dm} required by the system to achieve the target detection probability P_D can be inversely derived as the detection efficiency model:

$$N_{dm} = \frac{\ln(1 - P_D)}{\ln(1 - P_{hit})}. \tag{8}$$

It can be seen from the model that the higher the single effective detection probability Phit, the smaller the required number of accumulations and the higher the system detection efficiency. There are differences between single-echo and multi-echo array detectors in complex environments with foreground occlusion.

For long-range targets, the single-echo regime is easily triggered early by foreground noise or occluders and enters the dead-time blind zone, leading to a sharp decay in the capture probability of real distant targets and an exponential expansion of the required cumulative frames until detection failure. In contrast, the free-running mode effectively compensates for the probability loss caused by strong clutter through multiple state resets and probability decoupling after dead time [35,36]. It maintains a high-level single target capture probability even under complex building backgrounds, greatly reducing the cumulative frames required to achieve high confidence. The number of frames required to reach 95% confidence is shown in Figure 2, where the star markers indicate the first accumulated-frame positions at which each scheme reaches the 95% detection confidence threshold.

In urban low-altitude detection scenarios, small UAVs usually have extremely small laser scattering cross-sections and reflectivity, while their backgrounds are mostly highly reflective buildings. When a pixel field of view is partially occluded (i.e., part of the field of view corresponds to a small UAV in front and part corresponds to a highly reflective building behind the UAV), an extreme energy contrast of "weak front, strong rear" is formed. At this time, the target trigger probability evolution of the synchronous and free-running regimes is essentially different. The synchronous regime faces dual failure problems of near-field blocking and strong background submergence: the extremely high arrival rate of near-field clutter triggers the detector before the laser pulse reaches the UAV, resulting in near-zero target survival probability; even if some pulses penetrate near-field clutter, the detector is prone to miss detection due to Poisson distribution characteristics because of the weak UAV echo signal, and the non-triggered detector will eventually be triggered by the strong echo of the building behind. Therefore, in the single-echo regime, the capture probability of echo photons from a weak UAV target is extremely low and they are more easily masked by strong building background echoes. The free-running regime suppresses the influence of near-field clutter through short dead time: near-field clutter only consumes

the first trigger event, and the detector resets after dead time td to resume working before the UAV echo arrives, thus independently capturing the weak UAV echo. The strong echo of the building behind is recorded sequentially. The cumulative detection confidence under this small-UAV weak-echo scenario is further quantified in Figure 3, where the multi-echo regime requires only 26 accumulated frames to reach 95% confidence, while the single-echo regime requires 294 frames. This mode retains the intrinsic trigger probability of the UAV, providing key underlying data support for subsequent multi-frame accumulation and weak signal extraction via the waveform sequence convolution algorithm.

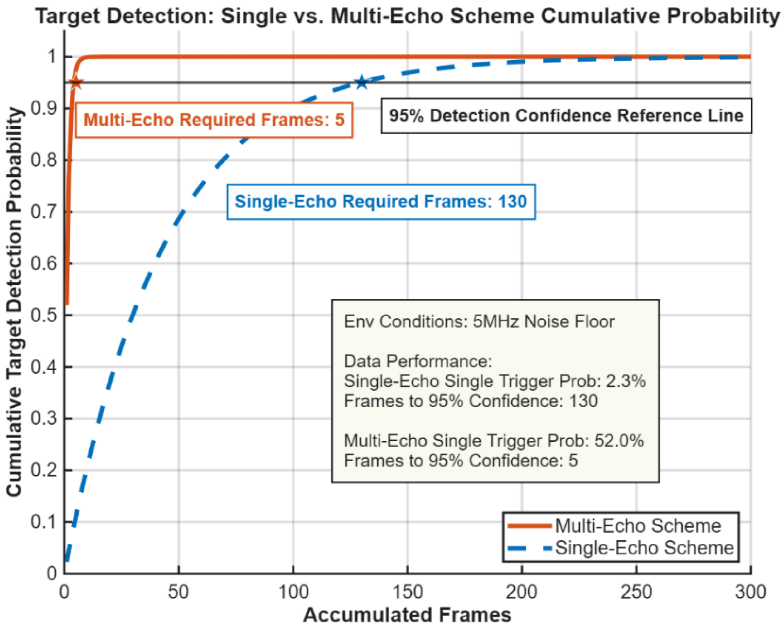


Figure 2. Single vs. multi-echo scheme cumulative probability.

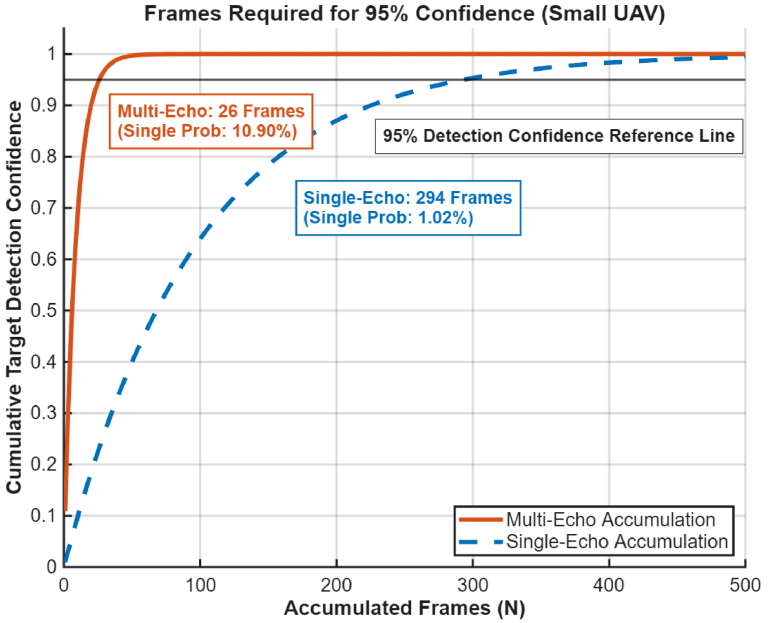


Figure 3. Frames required for 95% confidence (small UAV).

2.2. Anti-Interference Modulation via PPM Coding in Complex Backgrounds

To improve the cross-correlation between echo pulses and transmitted pulses and enhance the system's anti-interference capability under complex backgrounds with strong clutter such as buildings, this paper adopts the pulse position modulation (PPM) method

to modulate transmitted pulse signals. On the basis of the fixed repetition frequency of the transmitted laser, this method adds a random jitter within the modulation width to the pulse time position, which is generated by a local pseudo-random signal. Compared with other coding methods, PPM coding excited by pseudo-random signals has stronger randomness, better autocorrelation, and higher anti-interference capability [37]. PPM coding is simple, has low hardware requirements, good anti-noise interference capability, and solves the range ambiguity problem of high-repetition-frequency pulse ranging. The matching processing at the receiving end effectively extracts target echoes and suppresses background clutter uncorrelated with the coding. This processing helps improve the detection probability and detection stability of weak targets such as low-altitude UAVs under complex ground feature backgrounds.

PPM signals are realized through a closed-loop feedback structure. During modulation, the time interval value of adjacent pulses is first obtained according to the relational expression, then the timer starts counting. When the count value exceeds the output value, the pulse generator is triggered to generate a pulse. At the same time, the pulse is fed back to the counter module in a closed loop, resetting the counter to zero, and together with the pulse interval value forms the input of the module. The pulse interval generation module outputs again, and the above process is repeated until a complete PPM coded pulse sequence is output. Its principle is shown in Figure 4.

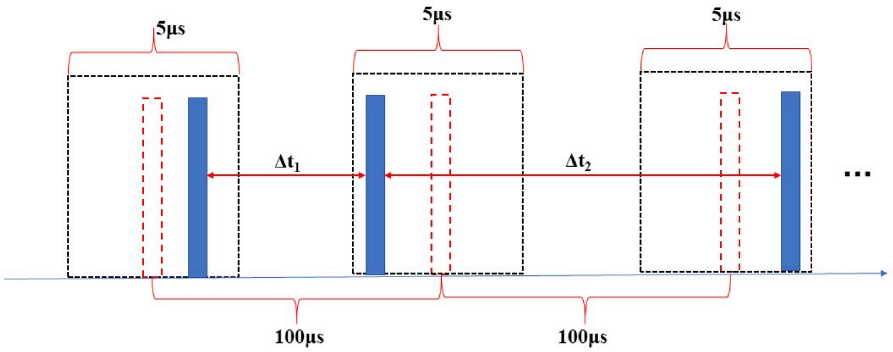


Figure 4. PPM is used to improve anti-interference capability. The dashed pulses correspond to a fixed repetition frequency of 10 kHz, and Δt is the actual pulse time interval, generated by modulation with a pseudo-random sequence. Black dashed rectangular boxes denote 100 μs detection frames with a 5 μs valid signal acquisition window; red dashed vertical lines represent transmitted laser pulses. The ellipsis "..." indicates continuous successive frame sequences.

Compared with the fixed repetition frequency transmission mode, pulse position coding modulation can effectively improve the system's anti-interference performance in strong background clutter. The echo signal of a low-altitude UAV target retains the coding timing structure of the transmitted pulses, only with an additional photon time-of-flight delay corresponding to the target distance. In contrast, background noise formed by sunlight scattering, building reflection, etc., usually has random temporal distribution and is uncorrelated with the PPM coding sequence.

Based on this, this paper realizes coherent demodulation of signals by performing matching convolution processing on the echo signals collected by the detector and the locally stored transmitted PPM sequence at the receiving end. When the coding segment in the echo is aligned with the reference sequence, the convolution output will show a significant correlation peak. The position of this peak corresponds to the photon time-of-flight of the target, thereby effectively extracting the weak echo information of low-altitude UAV targets from strong noise,

$$R_x(m - n_{lag}) = E[x(n)x(n - n_{lag} + m)] = \frac{1}{N}\sum_{n=1}^{N-m} x(n)x(n - n_{lag} + m). \quad (9)$$

Here, R_x represents the correlation degree between signal $x(n)$ and $x(n - n_{lag})$, and its correlation peak appears at the relative delay $m = n_{lag}$ of the two sequences, which is the photon time-of-flight of the target to be measured.

2.3. Building-Clutter Resilient Range Imaging Enhancement for PPM-Coded LiDAR

This paper proposes a UAV range imaging enhancement algorithm for PPM LiDAR under building backgrounds, which can adapt to strong building background echoes and natural light clutter interference, and effectively solve the weak target detection problem where UAVs occupy only a few pixels and their edge echo intensity is lower than the background. The algorithm roughly extracts candidate outlier points based on local outlier detection, eliminates single-frame isolated noise candidate points through temporal constraints, and then completes iterative optimization combined with Cell Averaging Constant False Alarm Rate (CA-CFAR) detection to achieve strong background suppression and UAV range image enhancement, finally outputting the target 3D pixel set. The overall flow is shown in Figure 5.

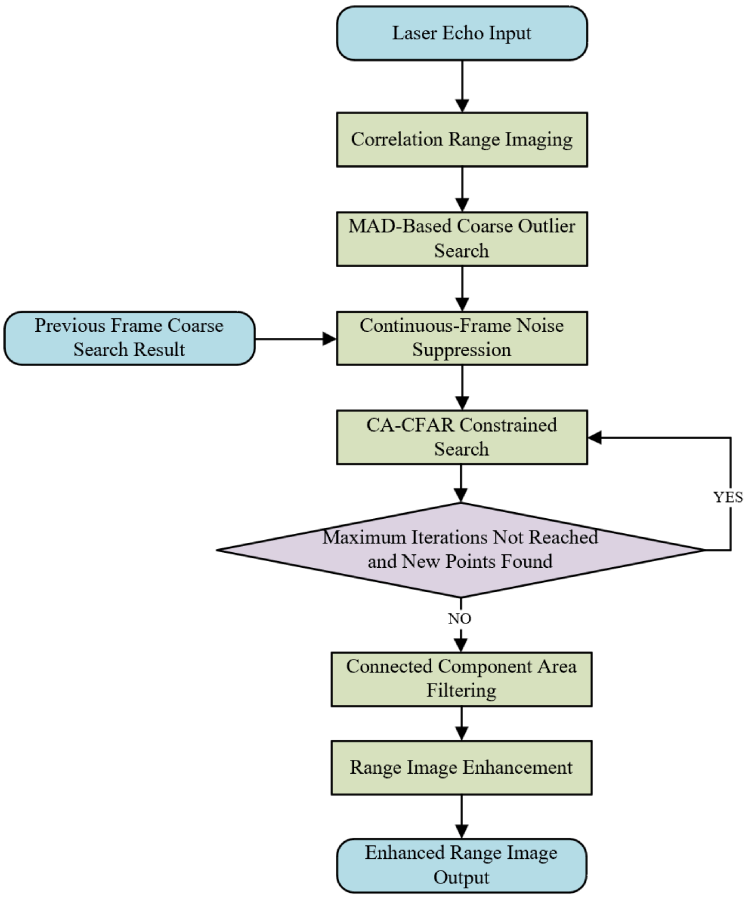


Figure 5. Algorithm flowchart. Light blue rounded boxes: input/output modules; light green rectangles: processing units; light purple diamond: judgment node. Solid black arrows show algorithm data flow; the YES branch loops back to the CA-CFAR Constrained Search step.

First, a preliminary range image **D** of the scene is obtained based on the correlation calculation of Equation (10). Since the UAV target only occupies 1 to 3 isolated pixels and its range characteristics are significantly different from the surrounding building background, this paper adopts the local Mean Absolute Deviation (MAD) algorithm for outlier detection

to roughly extract UAV candidate points from the strong background and initially segment potential target pixels. For each pixel (x, y) in the range image D, a 3×3 local neighborhood (i, j) is selected, and the local MAD value of the pixel is calculated based on the mean of the range values in the neighborhood to quantify the dispersion degree between the pixel range feature and the neighborhood background:

$$MAD(i,j) = \frac{1}{|N(i,j)|} \sum_{(x,y) \in N(i,j)} \left| \mathbf{D}(x,y) - \bar{\mathbf{D}}(x,y) \right|. \tag{10}$$

To achieve adaptive threshold screening, the MAD detection threshold is set to k times the global MAD mean. Combined with the feature that the UAV range value is slightly smaller than the background, when the MAD value of a pixel is greater than the threshold and the range value of the pixel is less than the background range, the pixel is judged as an outlier, i.e., a potential UAV candidate point. Finally, the initial candidate point set is roughly extracted, defined as:

$$\Omega_{init} = \{(i,j) | MAD(i,j) > \tau_{MAD}\}. \tag{11}$$

Background noise is easily misjudged as outliers. A significant feature of such noise points is that they only appear in a single frame without temporal continuity. As a moving target, the pixel position of a UAV maintains a certain correlation in two adjacent frames. Therefore, temporal constraints of range images between two consecutive frames are designed to eliminate single-frame isolated noise points and purify the candidate point set.

Let the current frame be t and the previous frame be $(t - 1)$. Local MAD outlier detection is performed on the two range images to obtain their respective initial candidate point sets $\Omega_{init,t}$ and $\Omega_{init,t-1}$. Considering that the UAV moves slowly with a small pixel position offset in two adjacent frames, the maximum motion offset is set $\Delta x, \Delta y \in [-1, 1]$. The inter-frame consistency judgment condition is defined as: for a current frame candidate point (i, j), there is at least one candidate point in the corresponding neighborhood of the previous frame. Candidate points satisfying the above inter-frame consistency condition are screened to obtain the purified UAV prior seed point set Ω_{seed}. Any point in the seed point set is used as the initial prior pixel of the UAV to slice in the original 3D point cloud data of the LiDAR. All points with a pixel interval from the seed point not greater than 1 and a z-axis distance difference not exceeding the threshold d_{max} are searched. The CA-CFAR detection mechanism is adopted for the slice, setting an adaptive threshold based on the statistical characteristics of background clutter to ensure effective capture of weak edge echoes of UAVs while suppressing building background clutter.

The slice is divided into voxels. Let the reference unit set be S_{ref} with quantity N_{ref}, and its echo intensity mean and variance be μ_{ref} and σ_{ref} 2. The CA-CFAR adaptive threshold is set as:

$$T_{CFAR} = \alpha \cdot (\mu_{ref} + \beta \cdot \sigma_{ref}), \tag{12}$$

where α and β are adjustment coefficients. If the detected voxel satisfies the echo intensity $I > T_{CFAR}$, the voxel is retained to generate a new point set Ω_{CFAR}. All seed points and different points are traversed to generate N connected domains. Iterative search is performed with the expanded seed until no new points are added. Since the UAV occupies very few pixels, the maximum number of iterations is set to 3, and targets with a pixel proportion greater than 20 pixels in all connected domains are deleted. During range imaging, the actual distance of pixels corresponding to the connected domain is taken as the distance corresponding to the maximum single-pixel intensity in the retained voxels, covering the corresponding pixels in $\mathbf{D}$. Finally, UAV range imaging enhancement under strong building backgrounds is realized, providing reliable support for subsequent target detection.

3. Experimental Results and Discussion

3.1. Parameter Analysis and Process Analysis of Enhancement Algorithm

To systematically investigate the influence of core hyperparameters on UAV target enhancement performance and formulate a standardized parameter tuning strategy, a high-fidelity simulation dataset featuring complex urban clutter and miniature UAV targets was constructed. Utilizing the Unity 3D simulation platform, high-precision geometric models of the targets and their surrounding environments were established to pre-generate full-field, high-resolution ground-truth maps of scene distance and surface reflectance. Figure 6 presents a representative rendering captured from the detector's viewpoint within the constructed virtual scene. Taking the accurate distance ground truth as input, we simulated the raw photon-counting echo signals collected by free-running single-photon LiDAR, where the temporal resolution of each independent sampling window was configured to 1 ns. After acquiring the raw photon measurement data, distance demodulation and 3D range image reconstruction were implemented to generate simulated depth images contaminated by building background clutter, which serve as the baseline dataset for parameter optimization and sensitivity analysis of the proposed enhancement algorithm.

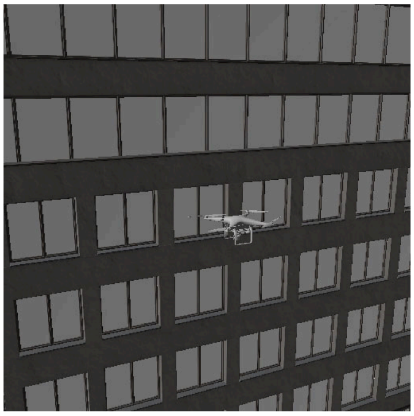


Figure 6. Unity 3D scene detector perspective example image.

The comprehensive operational pipeline of the proposed algorithm consists of several sequential processing stages, the intermediate visualization results of which are sequentially displayed in Figure 7. The procedure initiates with the reconstructed raw range map, followed by the calculation of a local MAD heatmap to construct a binary MAD mask governed by the threshold coefficient k. Next, a continuous-frame temporal suppression strategy utilizing an inter-frame depth constraint threshold d_{max} is adopted to eliminate stochastically isolated temporal clutter. Following the extraction of candidate seed points, a local neighborhood patch search is executed, and a CA-CFAR detector, modulated by the mean adjustment coefficient α and variance adjustment coefficient β, is applied to isolate the target from background structures, ultimately yielding the enhanced, high-fidelity depth image.

Within this framework, the local MAD detection threshold coefficient k dictates the stringency of filtering discrete candidate pixels. A smaller k corresponds to a lower detection threshold, whereas a larger k enforces more rigorous screening criteria. Since the introduced continuous-frame temporal constraint delivers robust false-alarm suppression against isolated single-frame noise, an excessively high screening threshold is unnecessary during the coarse extraction stage. Accordingly, k is constrained within the range of 1.2–2.0 to fully preserve the discrete edge pixels of low-SNR micro-UAV targets and prevent premature target elimination caused by rigid thresholds. When ambient optical noise intensifies, elevating the global MAD value and inducing massive spurious anomalies, k should be

moderately increased to lift the detection threshold and suppress redundant noise propagation. Conversely, under low-noise scenarios, a smaller k within the predefined boundaries can be adopted to maximize the detection probability of dim, small-scale targets.

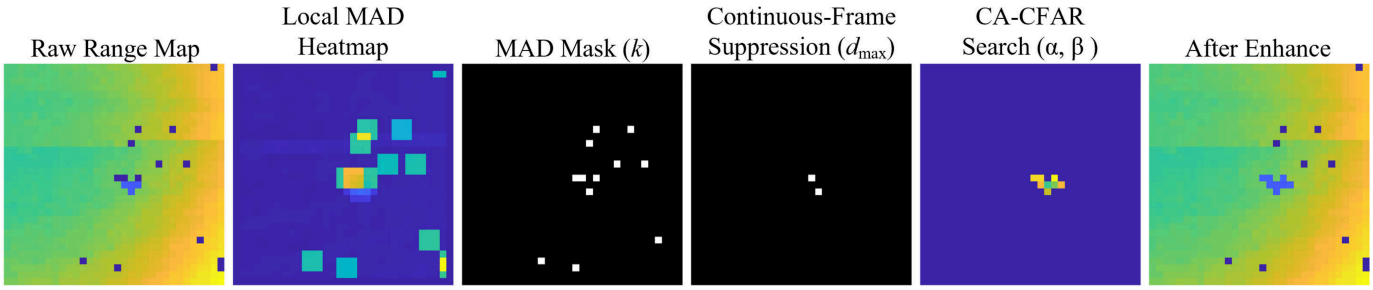


Figure 7. Intermediate processing results of the proposed enhancement algorithm. Subplots 1, 5 and 6 use colors to represent distance values, and subplot 2 reflects local MAD values. Blue represents low values and yellow represents high values in these subplots; white pixels in subplots 3 and 4 denote selected candidate points.

Furthermore, based on a joint physical constraint analysis incorporating the physical UAV size of 0.3 m and the laser pulse width of 10 ns, the inter-frame depth constraint threshold d_{max} is established at 3 m. This parameter defines the minimum spatial separation required for the algorithm to discriminate UAV targets from structural background clutter, such as building facades. It is worth noting that if the spatial margin between the target and the background wall falls below d_{max}, the iterative enhancement pipeline may fail to segregate the target from the clutter. For practical engineering deployment, this threshold should be minimized to the hardware's performance limit to boost detection adaptability for low-signature targets operating in close proximity to urban structures.

Following the temporal filtering phase, local patch searching is performed around the extracted seed points, where pixels with prominent echo intensity peaks are isolated via the CA-CFAR criterion, assuming the patch regions are clear of intense structural echoes by default. The mean adjustment coefficient α is calibrated based on the baseline noise floor, with α = 1.0 designated as the nominal operating standard. Under severe background noise fluctuations, α can be moderately enlarged to intensify static clutter suppression. Concurrently, since single-photon detection inherently suffers from severe random fluctuations and violent variance oscillations of clutter, a relatively large variance adjustment coefficient β is required. In this work, β is uniformly configured to 0.5 to ensure robust regularization across varying operating environments.

3.2. Simulation Comparative Experiments

Based on the pre-configured simulation dataset, comparative experiments are conducted to evaluate the performance of the proposed enhancement algorithm. The 3D range reconstruction results obtained under both the gate mode and the standard free-running mode are evaluated against the high-resolution ground truth. To benchmark our method against state-of-the-art single-photon restoration techniques, the free-running mode enhanced by the Markov correction algorithm is incorporated into the comparison. This baseline strictly adopts the exact waveform correction approach proposed by Lyu et al. [23] to compensate for the severe photon pile-up and dead-time distortions inherent in high-counting-rate free-running single-photon LiDAR. Lastly, qualitative and quantitative evaluations are performed across these modalities to comprehensively validate the superiority of the proposed algorithm.

It can be seen from the imaging results, as shown in Figure 8, that the scene contains both strong edge echo reflection components of small UAV targets and large-scale background echo components of buildings. The two echo signals are superimposed on each other. Under complex detection conditions with high background noise, echo waveform distortion and range peak aliasing are easily caused, making it difficult to accurately detect and distinguish the effective range peak of the target, eventually leading to target structure distortion, detail loss, and other problems.

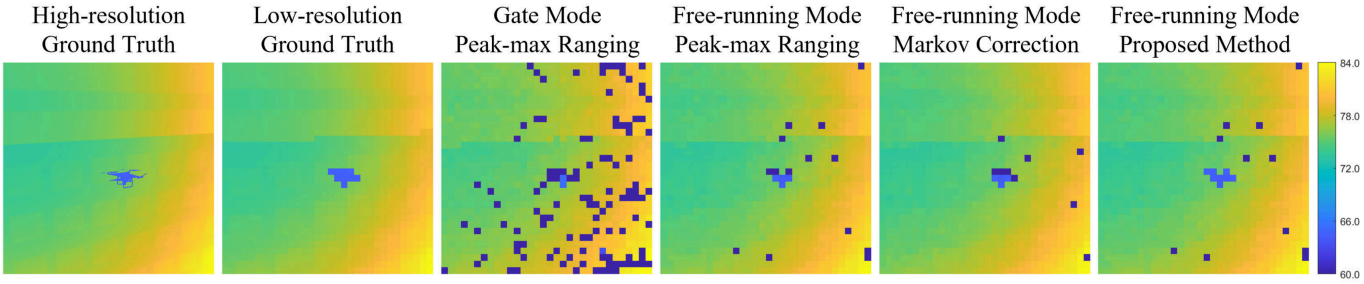


Figure 8. Distance imaging simulation qualitative comparison diagram. Colors represent distance values, with the color bar on the right indicating distance scales.

There is a large number of randomly discrete abnormal under-estimated pixels in the gate mode imaging results, with dense noise points and poor target contour integrity. In contrast, the free-running mode reconstruction results can effectively suppress large-scale random noise interference, and the restoration ability of the overall contour, edge detail texture of the UAV target, and background gradient change is significantly better than that of the synchronous detection mode. For the free-running mode with Markov correction, although it can further improve the overall reconstruction imaging performance and smooth the background clutter, it lacks targeted optimization for weak and small targets. Since the building wall echoes constitute the primary signal for the Markov correction algorithm, the weak echo variations in the miniature UAV cannot be effectively highlighted. In contrast, after introducing the proposed free-running mode enhancement algorithm, the enhanced reconstruction results can thoroughly suppress the remaining isolated noise interference and significantly strengthen the edge contour and detail texture features of the UAV target. Specifically, through targeted small target enhancement processing, the algorithm effectively enhances the overall contour clarity and edge detail texture recognition of the UAV target body. The proposed method can achieve accurate retention of UAV target features and greatly improved range imaging quality under severe scenes with strong building background echoes and multi-echo aliasing, verifying the excellent robustness and detail reconstruction advantages of the proposed free-running mode enhancement algorithm in single-photon ranging imaging under complex building backgrounds.

Unlike the Markov-corrected free-running mode, which improves overall reconstruction quality and smoothes background clutter yet fails to implement targeted optimization for dim small targets, the proposed enhancement algorithm realizes stable detection of UAV targets submerged under intense background interference. Equipped with dedicated small-target enhancement processing, the proposed method accurately retains UAV characteristic features and drastically boosts range imaging quality, even in harsh scenarios featuring severe building backscattering and multi-echo aliasing. These results sufficiently verify that the free-running enhancement strategy proposed in this paper possesses stronger robustness and better practical performance for single-photon LiDAR applied to complex urban low-altitude monitoring scenarios.

To quantitatively evaluate the actual optimization effect of the proposed algorithm, a data set is constructed and target detection boxes are annotated based on the complete simulation process, finally obtaining 2000 valid simulation samples. The data set is randomly divided into a training set and a test set at a ratio of 9:1, and training and testing experiments are carried out with the YOLOv11n model [38]. The improvement effect of the imaging method on target detection performance is comprehensively verified through three quantitative indicators, precision, recall, and mean Average Precision (mAP), where mAP@50 is based on an IOU of 50%. For the test set samples, the range truth map is first reduced to 32 × 32 size through pooling operation, and the corresponding coordinates of UAV targets in the image are annotated one by one. Based on the above coordinates, the Root Mean Square Error (RMSE) between the imaging results of different methods and the real range is calculated respectively. Considering that low SBR environments are prone to generate abnormal noise points, Imaging Accuracy (IA) is introduced as an auxiliary evaluation standard. The range imaging judgment rule is that when the error between the imaging range and the actual range is less than 3 m, it is judged as valid data; if the error exceeds the threshold, it is regarded as invalid range data that fails to solve the UAV laser echo normally.

The quantitative results shown in Table 1 demonstrate that compared with the gate mode, the free-running mode achieves significant improvements in ranging accuracy and detection performance. The gate mode has a high RMSE of 43.62 m and an imaging accuracy of only 21.36%, severely affected by noise and multi-echo aliasing; the free-running mode before enhancement reduces the RMSE to 34.04 m, improves the imaging accuracy to 52.78%, and increases the detection mAP@50 from 65.16% to 77.78%, indicating that the free-running regime can effectively suppress noise and improve the reliability of range solution. Furthermore, the Markov correction method reduces the RMSE to 3.31 m, and improves the imaging accuracy and precision to 74.02% and 82.15%, respectively, due to its excellent recovery of large-scale background structures. However, in overlapping echo regions where both the UAV and the wall exist, general optimization algorithms treat the strong wall echoes as the dominant signal. This causes the optimization process to preferentially reconstruct the background wall behind the target, making it even easier to bury the weak UAV compared to raw peak searching, thus limiting its recall 68.72% and mAP@50 77.41%. After processing by the proposed free-running mode enhancement algorithm, the RMSE is also significantly reduced to 3.64 m, the imaging accuracy reaches 71.49%, and notably, the recall 73.32% and mAP@50 80.05% achieve the optimal values among all methods. This demonstrates that the proposed method can significantly suppress abnormal errors by specifically optimizing and highlighting weak target features against strong background reflections, providing more accurate input for target detection.

Table 1. Comparison of quantitative results table.

Mode	RMSE (m)	IA (%)	P (%)	R (%)	mAP@50 (%)
Gatemode	43.62	21.36	73.02	62.49	65.16
Before enhancing free mode	34.04	52.78	79.33	70.66	77.78
Markov correction	3.31	74.02	82.15	68.72	77.41
Proposed Method	3.64	71.49	81.47	73.32	80.05

From the detection effect, the gate mode has dense noise and many abnormal points, blurred target contours, and is prone to false and missed detections. As shown in Figure 9, the free-running mode before enhancement greatly reduces discrete noise and has a cleaner background and a more complete UAV contour, significantly reducing detection difficulty.

For the free-running mode with Markov correction, although the background noise is further suppressed, the algorithm tends to optimize toward the strong background wall echoes in multi-echo regions, thereby preferentially restoring the wall while smoothing out the overlapping weak UAV target. This leads to severe missed detections or degraded bounding box positioning for small UAVs, yielding a lower recall performance. After free-running mode enhancement by the proposed method, the edge and geometric structure of the UAV target are further highlighted, with clear UAV morphology and significant features, more accurate detection box positioning, and higher confidence. The results show that the proposed method effectively improves imaging quality through dual optimization of detection method and enhancement algorithm, with obvious positive gains for subsequent target detection tasks.

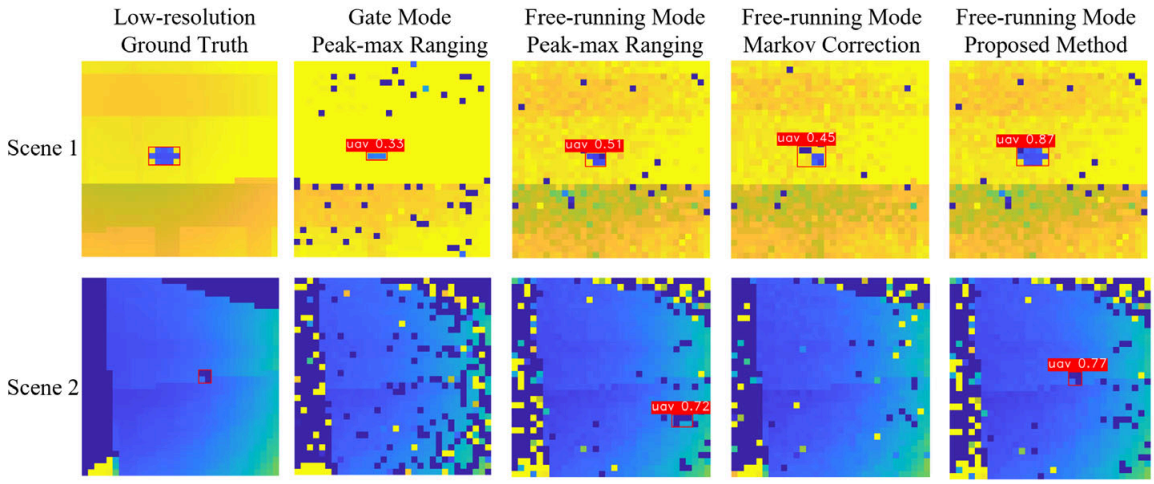


Figure 9. YOLOv11n comparison chart of test results. Red boxes denote detection outputs from YOLO, and the values above each box represent target confidence scores; colors correspond to distance values.

3.3. Experimental System

The single-photon LiDAR experimental system constructed in this paper is centered on a free-asynchronous running mode Geiger-mode avalanche photodiode array, and its structural block diagram is shown in Figure 10. The transmitter module uses a fiber laser with a wavelength of 1064 nm, a repetition frequency of 10 kHz, and a pulse width of 10 ns as the light source. To improve the capture and tracking capability of maneuvering targets, the system integrates a dual fast steering mirror subsystem with co-aperture transmission and reception. Based on the real-time acquired target position prediction information, this subsystem realizes synchronous and high-speed servo control of the outgoing laser beam pointing and receiving field of view. The 12-bit m-sequence-based pseudo-random PPM encoding, controlled by the XCKU115 FPGA (Xilinx Inc., San Jose, CA, USA), operates within a range of 0–4096 ns. In the receiving optical path, a narrow-band spectral filter (central wavelength 1064 nm, bandwidth 2 nm) is used to effectively suppress background light noise of non-signal wavelengths. The detector module adopts a 32 × 32-pixel single-photon area array, operating in free-running mode, with low temporal jitter and high detection efficiency. The acquisition module consists of a time-to-digital converter array and FPGA, which is used to record the precise arrival time of each valid photon event and transmit it to the host computer in real time for signal processing and target solution.

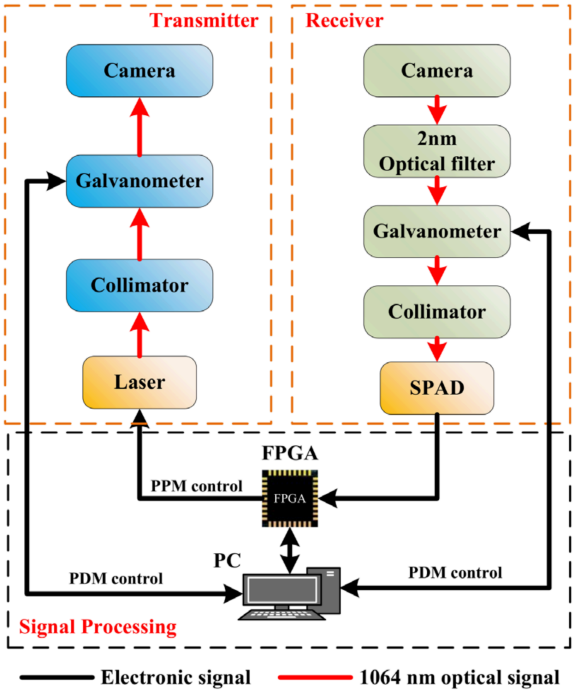


Figure 10. Experimental system architecture diagram.

3.4. Field Test Verification

To evaluate the actual detection and tracking performance of the constructed single-photon LiDAR system for low-altitude, slow, small (LSS) UAV targets in the urban building background environment, field experiments are carried out in this paper. A typical commercial quadrotor UAV (DJI Phantom 3, DJI, Shenzhen, China) is used as the detection target, and it is placed in front of a high-rise building group with dense and complex geometric structures for flight. The building group generates strong, non-uniform background laser echoes, forming a detection environment with an extremely low SBR, aiming to simulate a real urban key area air defense scenario. Figures 11 and 12 show the experimental scene and the visible-light camera footage of the UAV detection target under different background noise conditions.

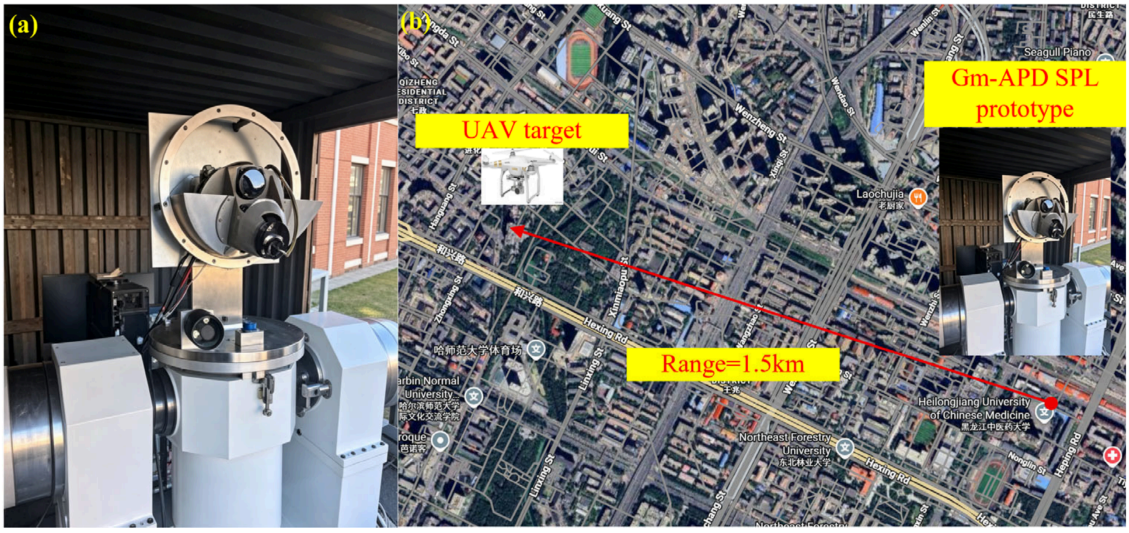


Figure 11. Schematic diagram of detecting low-altitude UAV targets. (**a**) Single-photon LiDAR system prototype. (**b**) Experimental scene.

To verify the improvement effect of the proposed building background PPM LiDAR UAV range imaging enhancement algorithm on target detection and imaging performance, a comparative verification is carried out under a unified experimental platform and scene in this section. Both groups of experiments adopt the proposed pseudo-random PPM transmission mechanism and waveform sequence convolution matching detection algorithm, with differences only in the back-end imaging processing link. The first group only performs PPM coding waveform convolution processing without adding the range imaging enhancement link; the second group further adopts the proposed range imaging enhancement algorithm on the basis of PPM convolution processing, realizing strong clutter suppression and UAV target range image enhancement through the joint optimization of local outlier detection, temporal constraint purification, and CA-CFAR constant false alarm detection. Both groups of experiments use the same free-running SPAD array detector, the same transmission parameters, and the same high-rise building background low-altitude UAV scene, obtaining echo photon events and inverting them to generate 2D intensity images and range images.

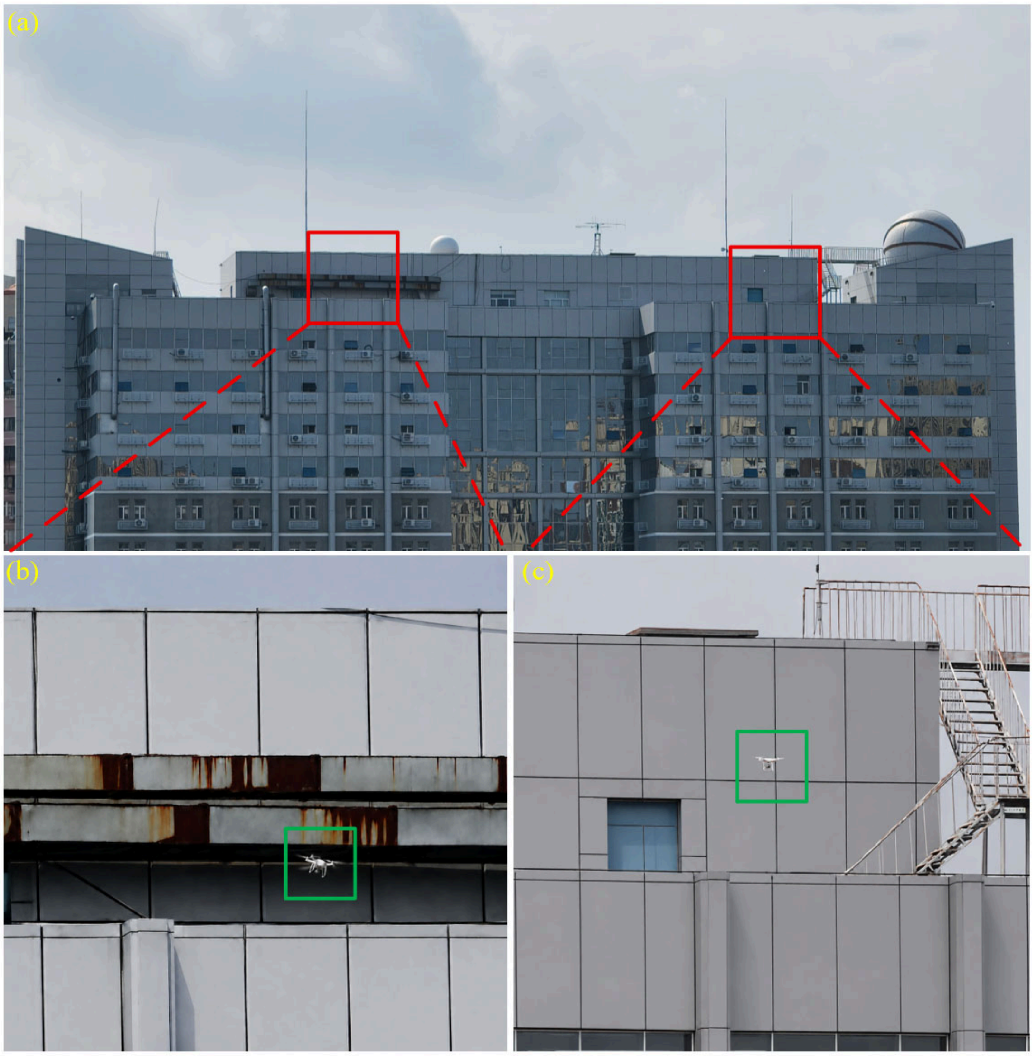


Figure 12. Overview and local magnified views of the experimental scene. (**a**) Panorama of the building background with red frames marking the regions of interest. (**b**) Magnified view of the left pipeline region on a sunny morning. (**c**) Magnified view of the right staircase region on an overcast morning. (Target UAVs are highlighted in green boxes).

Comparing the range images before and after enhancement in Figure 13, it can be seen that although the basic algorithm based on PPM coding has effectively suppressed most of the background clutter, the hovering UAV target in both the pipeline scene (a) and the staircase scene (b) appears as only two and a single isolated pixel point, respectively, with extremely low contour recognition, which is easily misjudged as a noise point. Because the pipeline scene (a) is performed under conditions with relatively strong background noise, the overall scene reconstruction is not fully complete. After introducing the proposed building background range imaging enhancement algorithm, the effective pixels in the target areas of both scenes are significantly expanded, forming clearly distinguishable target clusters, and the contour integrity and feature recognition are greatly improved. While maintaining the background suppression capability, the enhancement algorithm effectively restores the basic morphological characteristics of the UAV target through small target enhancement and local consistency processing, avoiding the risk of missed detection of single-pixel targets. The results show that the enhancement algorithm can significantly improve the imaging quality and target detection stability of PPM-coded LiDAR for low-altitude weak UAV targets under strong building clutter backgrounds, verifying its excellent target enhancement capability and robustness in complex building scenes.

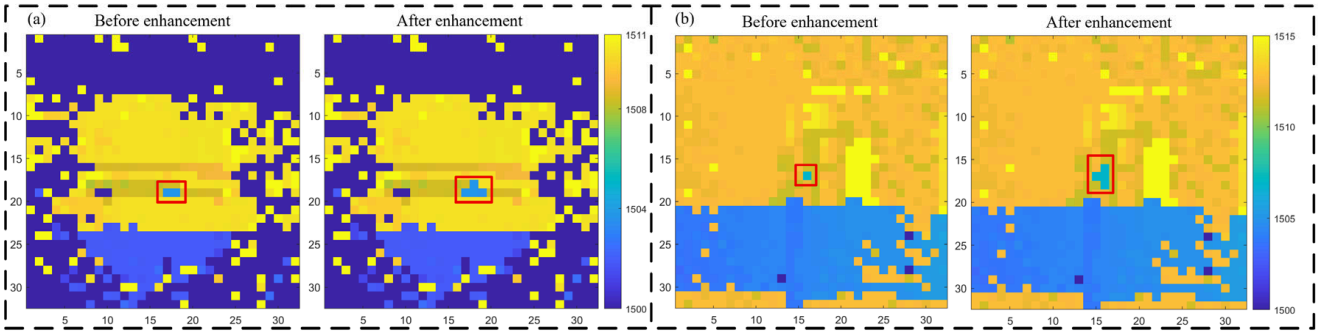


Figure 13. Comparison of real experimental range images of a hovering UAV before and after enhancement. (**a**) Pipeline scene under strong background noise. (**b**) Staircase scene. The red frame marks the region of the UAV, and colors represent distance values.

Furthermore, to validate the algorithm's continuous tracking capability, echo data were acquired over consecutive time intervals, and identical processing procedures were applied to generate UAV range profiles frame by frame for both the pipeline and staircase scenes, as shown in Figure 14. As observed in the original imaging results in Figure 14a, due to the suppression of strong background clutter, the moving UAV target appears as weak, isolated pixels that shift positions across consecutive frames, which easily leads to tracking intermission or track loss in practical applications. After applying the proposed enhancement algorithm, as shown in Figure 14b, the weak echoes of the dynamic UAV are consistently highlighted and expanded into distinct multi-pixel clusters in each sequential frame, successfully preserving the target's motion trajectory. The experimental results indicate that the established system can reliably achieve continuous tracking and precise detection of small-scale UAVs. Compared with traditional techniques, the integration of PPM and the range imaging enhancement algorithm yields superior imaging fidelity for low-altitude targets operating against complex building backgrounds. By restoring the morphological characteristics of weak UAV echoes, the proposed method substantially reduces the risk of missed detection, thereby providing a critical prerequisite for stable long-term tracking and surveillance applications.

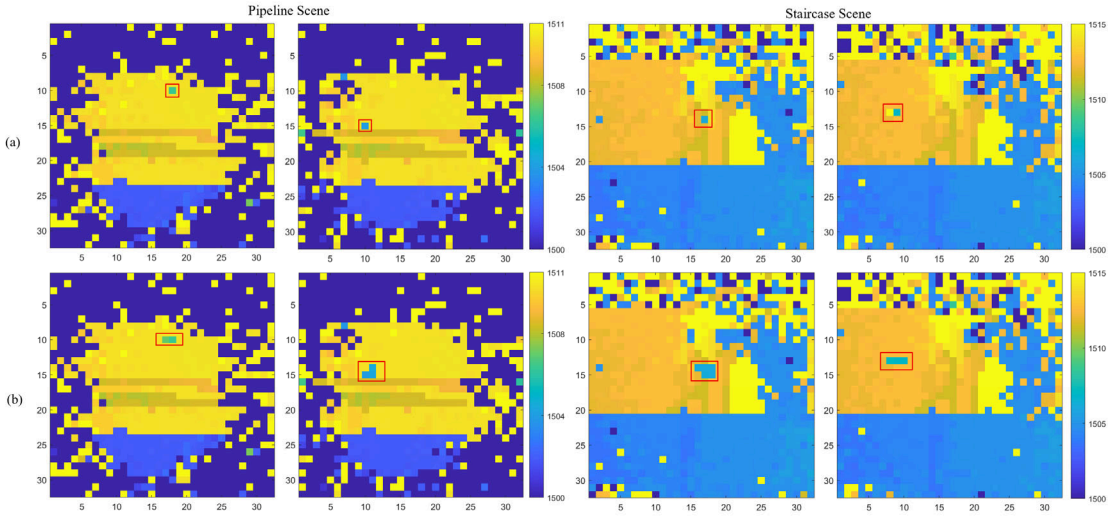


Figure 14. Real experimental range images of dynamic UAV tracking over consecutive frames. (**a**) Original imaging and (**b**) enhanced imaging for both the pipeline scene (left columns) and staircase scene (right columns). The red frame marks the region of the UAV, and colors represent distance values.

4. Conclusions

To address the challenges of weak and easily masked echoes from low-altitude LSS UAVs, as well as the limitations of conventional single-photon detection in dense urban clutter, this paper proposes a UAV detection framework based on free-running single-photon detection and PPM-coded LiDAR. We construct a free-running single-photon detection system that integrates a free-running operational regime, pseudo-random PPM, and waveform convolution matching, complemented by a building-clutter-oriented range imaging enhancement algorithm. Validated through theoretical analysis, Unity 3D simulations, and field experiments, the proposed method reduces the RMSE from 43.62 m to 3.64 m compared with the traditional gated mode. Crucially, while the popular Markov correction method preferentially reconstructs strong building structure background echoes and tends to submerge weak targets in multi-echo overlapping regions, the proposed algorithm effectively preserves small-target features. Ultimately, it achieves the optimal detection performance among all compared methods, yielding a recall of 73.32% and an mAP@50 of 80.05%, which marks a substantial improvement over the 65.16% exhibited by the traditional gated mode. The results demonstrate that this method effectively suppresses strong building reflections and environmental noise, reliably extracts weak UAV signals under extremely low SBR, and achieves stable low-altitude UAV detection at 1.5 km. Characterized by robust anti-interference capabilities and high imaging accuracy, this scheme provides critical technical support for LSS UAV detection in urban air defense and security surveillance.

Author Contributions: Conceptualization, Y.W. and X.Z.; methodology, Y.W.; software, Y.W. and Z.T.; validation, Y.W., R.Y. and J.G.; formal analysis, J.G.; investigation, J.G.; resources, Y.W.; data curation, Y.W.; writing—original draft preparation, Y.W.; writing—review and editing, Y.W.; visualization, Z.Y.; supervision, J.Z. and Y.Z.; project administration, Y.W.; funding acquisition, X.Z. All authors have read and agreed to the published version of the manuscript.

Funding: This research received no external funding.

Data Availability Statement: The raw data supporting the conclusions of this article will be made available by the authors on request.

Conflicts of Interest: The authors declare no conflict of interest.

Abbreviations

The following abbreviations are used in this manuscript:

UAV	Unmanned Aerial Vehicle
LiDAR	Light Detection and Ranging
SPAD	Single-Photon Avalanche Diode
SBR	Signal-to-Background Ratio
PPM	Pulse Position Modulation
CA-CFAR	Cell Averaging Constant False Alarm Rate
MAD	Mean Absolute Deviation
RMSE	Root Mean Square Error
IA	Imaging Accuracy
mAP	mean Average Precision
FPGA	Field Programmable Gate Array
LSS	Low, Slow, and Small

References

1. Zhang, H.; Cao, C.; Xu, L.; Gulliver, T.A. A UAV Detection Algorithm Based on an Artificial Neural Network. *IEEE Access* **2018**, *6*, 24720–24728. [CrossRef]
2. Swatantran, A.; Tang, H.; Barrett, T.; DeCola, P.; Dubayah, R. Rapid, High-Resolution Forest Structure and Terrain Mapping over Large Areas Using Single Photon Lidar. *Sci. Rep.* **2016**, *6*, 28277. [CrossRef] [PubMed]
3. Chen, Z.; Miao, Y.; Tang, D.; Yang, H.; Pan, W. Effect of Lidar Receiver Field of View on UAV Detection. *Photonics* **2022**, *9*, 972. [CrossRef]
4. Liu, Y.; Chi, K.; Xue, R.; Huang, G. 3D Reconstruction Method for GM-APD Array LiDAR Based on Intensity Image Guidance. *Photonics* **2026**, *13*, 323. [CrossRef]
5. Fang, Y.-Q.; Chen, W.; Ao, T.-H.; Liu, C.; Wang, L.; Gao, X.-J.; Zhang, J.; Pan, J.-W. InGaAs/InP Single-Photon Detectors with 60% Detection Efficiency at 1550 Nm. *Rev. Sci. Instrum.* **2020**, *91*, 083102. [CrossRef] [PubMed]
6. Kirmani, A.; Venkatraman, D.; Shin, D.; Colaço, A.; Wong, F.N.C.; Shapiro, J.H.; Goyal, V.K. First-Photon Imaging. *Science* **2014**, *343*, 58–61. [CrossRef] [PubMed]
7. Shin, D.; Kirmani, A.; Goyal, V.K.; Shapiro, J.H. Photon-Efficient Computational 3-D and Reflectivity Imaging With Single-Photon Detectors. *IEEE Trans. Comput. Imaging* **2015**, *1*, 112–125. [CrossRef]
8. Shin, D.; Xu, F.; Venkatraman, D.; Lussana, R.; Villa, F.; Zappa, F.; Goyal, V.K.; Wong, F.N.C.; Shapiro, J.H. Photon-Efficient Imaging with a Single-Photon Camera. *Nat. Commun.* **2016**, *7*, 12046. [CrossRef] [PubMed]
9. Shin, D.; Kirmani, A.; Goyal, V.K.; Shapiro, J.H. Computational 3D and Reflectivity Imaging with High Photon Efficiency. In Proceedings of the 2014 IEEE International Conference on Image Processing (ICIP), Paris, France, 27–30 October 2014; pp. 46–50.
10. Beer, M.; Schrey, O.M.; Haase, J.F.; Ruskowski, J.; Brockherde, W.; Hosticka, B.J.; Kokozinski, R. SPAD-Based Flash LiDAR Sensor with High Ambient Light Rejection for Automotive Applications. In *Proceedings of the Quantum Sensing and Nano Electronics and Photonics XV, San Francisco, CA, USA, 28 January–2 February 2018*; SPIE: Bellingham, WA, USA, 2018; Volume 10540, pp. 320–327.
11. Rapp, J.; Goyal, V.K. A Few Photons Among Many: Unmixing Signal and Noise for Photon-Efficient Active Imaging. *IEEE Trans. Comput. Imaging* **2017**, *3*, 445–459. [CrossRef]
12. Li, Z.P.; Huang, X.; Cao, Y.; Wang, B.; Li, Y.H.; Zhang, J.; Zhang, Q.; Peng, C.-Z.; Xu, F.; Pan, J.W. All-Time Single-Photon 3D Imaging Over 21 Km. In Proceedings of the 2019 Conference on Lasers and Electro-Optics (CLEO), San Jose, CA, USA, 5–10 May 2019; pp. 1–2.
13. Wang, M.; Sun, J.; Li, S.; Lu, W.; Zhou, X.; Zhang, H. A Photon-Number-Based Systematic Algorithm for Range Image Recovery of GM-APD Lidar under Few-Frames Detection. *Infrared Phys. Technol.* **2022**, *125*, 104267. [CrossRef]
14. Halimi, A.; Maccarone, A.; Lamb, R.A.; Buller, G.S.; McLaughlin, S. Robust and Guided Bayesian Reconstruction of Single-Photon 3D Lidar Data: Application to Multispectral and Underwater Imaging. *IEEE Trans. Comput. Imaging* **2021**, *7*, 961–974. [CrossRef]
15. Yurtsever, E.; Lambert, J.; Carballo, A.; Takeda, K. A Survey of Autonomous Driving: Common Practices and Emerging Technologies. *IEEE Access* **2020**, *8*, 58443–58469. [CrossRef]
16. Siegmund, O.H.W.; McPhate, J.; Tremsin, A.; Vallerga, J.V.; Welsh, B.Y.; Wheatley, J.M. High Time Resolution Astronomical Observations with the Berkeley Visible Image Tube. *AIP Conf. Proc.* **2008**, *984*, 103–114. [CrossRef]
17. Li, Z.-P.; Huang, X.; Cao, Y.; Wang, B.; Li, Y.-H.; Jin, W.; Yu, C.; Zhang, J.; Zhang, Q.; Peng, C.-Z.; et al. Single-Photon Computational 3D Imaging at 45 Km. *Photon. Res.* **2020**, *8*, 1532–1540. [CrossRef]

18. Li, Z.-P.; Ye, J.-T.; Huang, X.; Jiang, P.-Y.; Cao, Y.; Hong, Y.; Yu, C.; Zhang, J.; Zhang, Q.; Peng, C.-Z.; et al. Single-Photon Imaging over 200 km. *Optica* **2021**, *8*, 344–349. [CrossRef]
19. Kirchner, G.; Koidl, F.; Friederich, F.; Buske, I.; Völker, U.; Riede, W. Laser Measurements to Space Debris from Graz SLR Station. *Adv. Space Res.* **2013**, *51*, 21–24. [CrossRef]
20. Hampf, D.; Niebler, F.; Meyer, T.; Riede, W. The miniSLR: A Low-Budget, High-Performance Satellite Laser Ranging Ground Station. *J. Geod.* **2024**, *98*, 8. [CrossRef]
21. Sun, X.; Yan, H.; He, H.; Kong, X.; Mao, C.; Yan, F. Comparative Analysis of Free-Running and Gating Imaging Modes of SPAD Sensors. *Photonics* **2024**, *11*, 721. [CrossRef]
22. Yu, M.; Shi, M.; Hu, W.; Yi, L. FPGA-Based Dual-Pulse Anti-Interference Lidar System Using Digital Chaotic Pulse Position Modulation. *IEEE Photonics Technol. Lett.* **2021**, *33*, 757–760. [CrossRef]
23. Lyu, L.; Li, D.; Wu, T.; Mi, Q.; Yang, Y.; Zhou, W.; Xu, L. High-Counting-Rate Single-Photon LiDAR With Free-Running InGaAs/InP SPAD. *IEEE Trans. Instrum. Meas.* **2025**, *74*, 9537812. [CrossRef]
24. Li, Y.; Ye, W.; Li, Z.; Long, M.; Wu, Z.; Cao, Y.; Peng, C.; Xu, F. Compact Single-Photon LiDAR for Satellite Laser Ranging. *Opt. Express* **2025**, *33*, 40876–40890. [CrossRef] [PubMed]
25. Li, Z.; Lai, J.; Wang, C.; Yan, W.; Li, Z. Influence of Dead-Time on Detection Efficiency and Range Performance of Photon-Counting Laser Radar That Uses a Geiger-Mode Avalanche Photodiode. *Appl. Opt.* **2017**, *56*, 6680–6687. [CrossRef] [PubMed]
26. Gatt, P.; Johnson, S.; Nichols, T. Dead-Time Effects on Geiger-Mode APD Performance. In *Laser Radar Technology and Applications XII*; SPIE: Bellingham, WA, USA, 2007; Volume 6550, p. 65500I.
27. Du, B.; Pang, C.; Wu, D.; Li, Z.; Peng, H.; Tao, Y.; Wu, E.; Wu, G. High-Speed Photon-Counting Laser Ranging for Broad Range of Distances. *Sci. Rep.* **2018**, *8*, 4198. [CrossRef] [PubMed]
28. Pawlikowska, A.M.; Halimi, A.; Lamb, R.A.; Buller, G.S. Single-Photon Three-Dimensional Imaging at up to 10 Kilometers Range. *Opt. Express* **2017**, *25*, 11919–11931. [CrossRef] [PubMed]
29. Pediredla, A.K.; Sankaranarayanan, A.C.; Buttafava, M.; Tosi, A.; Veeraraghavan, A. Signal Processing Based Pile-up Compensation for Gated Single-Photon Avalanche Diodes. *arXiv* **2018**, arXiv:1806.07437.
30. Pellegrini, S.; Buller, G.S.; Smith, J.M.; Wallace, A.M.; Cova, S. Laser-Based Distance Measurement Using Picosecond Resolution Time-Correlated Single-Photon Counting. *Meas. Sci. Technol.* **2000**, *11*, 712. [CrossRef]
31. Antolovic, I.M.; Burri, S.; Bruschini, C.; Hoebe, R.; Charbon, E. Nonuniformity Analysis of a 65-Kpixel CMOS SPAD Imager. *IEEE Trans. Electron Devices* **2016**, *63*, 57–64. [CrossRef]
32. Antolovic, I.M.; Bruschini, C.; Charbon, E. Dynamic Range Extension for Photon Counting Arrays. *Opt. Express* **2018**, *26*, 22234–22248. [CrossRef] [PubMed]
33. Rapp, J.; Ma, Y.; Dawson, R.M.A.; Goyal, V.K. Dead Time Compensation for High-Flux Ranging. *IEEE Trans. Signal Process.* **2019**, *67*, 3471–3486. [CrossRef]
34. Zhang, G.; Lian, W.; Li, S.; Cui, H.; Jing, M.; Chen, Z. A Self-Adaptive Denoising Algorithm Based on Genetic Algorithm for Photon-Counting Lidar Data. *IEEE Geosci. Remote Sens. Lett.* **2022**, *19*, 6501405. [CrossRef]
35. Boretti, A. A Perspective on Single-Photon LiDAR Systems. *Microw. Opt. Technol. Lett.* **2024**, *66*, e33918. [CrossRef]
36. Hou, A.; Hu, Y.; Xie, Y.; Zhao, N.; Xu, S.; Wang, Y.; Zhang, X.; Han, F.; Fang, J. Full Waveform Recovery Method of Moving Target for Photon Counting Lidar. *IEEE Trans. Geosci. Remote Sens.* **2024**, *62*, 5701114. [CrossRef]
37. Gatt, P.; Johnson, S.; Nichols, T. Geiger-Mode Avalanche Photodiode Ladar Receiver Performance Characteristics and Detection Statistics. *Appl. Opt.* **2009**, *48*, 3261–3276. [CrossRef] [PubMed]
38. Khanam, R.; Hussain, M. YOLOv11: An Overview of the Key Architectural Enhancements. *arXiv* **2024**, arXiv:2410.17725.

Disclaimer/Publisher's Note: The statements, opinions and data contained in all publications are solely those of the individual author(s) and contributor(s) and not of MDPI and/or the editor(s). MDPI and/or the editor(s) disclaim responsibility for any injury to people or property resulting from any ideas, methods, instructions or products referred to in the content.